



Boosting ethanol oxidation by NiOOH-CuO nano-heterostructure for energy-saving hydrogen production and biomass upgrading

Hainan Sun^a, Lili Li^b, Yahui Chen^c, Hyunseung Kim^a, Xiaomin Xu^d, Daqin Guan^e, Zhiwei Hu^f, Linjuan Zhang^{b,*}, Zongping Shao^{d,g,**}, WooChul Jung^{a,*}

^a Department of Materials Science and Engineering, Korea Advanced Institute of Science and Technology (KAIST), Daejeon 34141, Republic of Korea

^b Key Laboratory of Interfacial Physics and Technology, Shanghai Institute of Applied Physics, Chinese Academy of Sciences, Shanghai 201800, PR China

^c Department of Chemistry and Nanoscience, Ewha Womans University, Seoul 03760, Republic of Korea

^d WA School of Mines: Minerals Energy and Chemical Engineering (WASM-MECE), Curtin University, Perth, Western Australia 6102, Australia

^e Department of Building and Real Estate, The Hong Kong Polytechnic University, Hung Hom, Kowloon 999077, Hong Kong, China

^f Affiliation Max Planck Institute for Chemical Physics of Solids, Nöthnitzer Strasse 40, Dresden 01187, Germany

^g State Key Laboratory of Materials-Oriented Chemical Engineering, College of Chemical Engineering, Nanjing Tech University, Nanjing 211816, PR China

ARTICLE INFO

Keywords:

3d transition metal
Nano-heterostructure
Ethanol oxidation reaction
Value-added chemicals
Hydrogen production

ABSTRACT

Substituting the anodic oxygen evolution reaction in water electrolysis with a thermodynamically more favorable ethanol oxidation reaction (EOR) provides a promising route for simultaneous biomass upgrading and energy-saving hydrogen production. Herein, we synthesize a NiOOH-CuO nano-heterostructure anchored on a three-dimensional conductive Cu foam, which exhibits remarkable EOR performance, surpassing all the state-of-the-art 3d transition-metal-based EOR electrocatalysts. Density functional theory reveals that the coupling between CuO and NiOOH by charge redistribution at the interface is critical, synergistically reducing the EOR energy barriers into an energetically favorable pathway. Conclusively, the hybrid water electrolysis cell using our catalyst as the anode (1) requires only a low cell voltage for H₂ generation at the cathode and only liquid chemical production of acetate at the anode, and (2) shows a high ethanol conversion rate to acetate, which can readily be separated from the aqueous electrolyte by subsequent acidification and extraction processes.

1. Introduction

The distinct advantages of high energy density and environmental friendliness make hydrogen (H₂) a promising energy carrier and fuel [1, 2]. Hydrogen production by electrochemical water splitting conducted at low temperatures has attracted extensive attention [3–5]. However, the overall efficiency of traditional water electrolysis is largely determined by the sluggish kinetics of the anodic reaction, that is, the oxygen evolution reaction (OER) [6,7]. In particular, the alkaline OER rate is constrained by the adsorption-energy scaling relations involving multiple reaction intermediates of MOOH, MO, and MOH (where M represents the surface active site) [8]. As a result, a minimum theoretical overpotential of approximately 370 mV is required for alkaline OER even when using electrocatalysts with ideal reactivity, such as Ir(Ru)O_x and NiFeO_x [2,8,9].

On the one hand, methods of overcoming, breaking, or even bypassing the scaling relations to reduce the anodic overpotential in water splitting have become a popular research topic [8,10]. On the other hand, replacing the OER with other readily available anodic reactions also provides a promising opportunity to reduce the potential for hydrogen production and overall energy consumption [11]. Practically, electrocatalysis of compounds such as urea, glycerol, and hydrazine, and even biomass-related chemicals such as methanol, ethanol, benzyl alcohol, and 5-hydroxymethylfurfural has received extensive attention from researchers because the anodic conversion of these chemicals usually occurs at an equilibrium potential lower than the OER does [11–16]. More importantly, this strategy not only further saves the energy required to produce hydrogen at the cathode, but also allows the simultaneous synthesis of high-value chemical at the anode. Biomass-related chemicals, such as methanol, ethanol, benzyl alcohol,

* Corresponding authors.

** Corresponding author at: WA School of Mines: Minerals Energy and Chemical Engineering (WASM-MECE), Curtin University, Perth, Western Australia 6102, Australia.

E-mail addresses: zhanglinjuan@sinap.ac.cn (L. Zhang), shaozp@njtech.edu.cn (Z. Shao), wjchung@kaist.ac.kr (W. Jung).

<https://doi.org/10.1016/j.apcatb.2023.122388>

Received 13 September 2022; Received in revised form 21 December 2022; Accepted 5 January 2023

Available online 7 January 2023

0926-3373/© 2023 Elsevier B.V. All rights reserved.

and 5-hydroxymethylfurfural, are good candidates for such hybrid water electrolysis [11]. Ethanol ($\text{C}_2\text{H}_5\text{OH}$), traditionally derived from the hydration of ethylene or biomass fermentation, is considered a valuable upgraded byproduct with high energy density (21 MJ L^{-1}), low cost, and low toxicity [11,17]. Moreover, ethanol can also serve as a precursor for producing fine chemicals, such as acetate, acetaldehyde, ethyl acetate, and 1,1-diethoxyethane [18,19]. The ethanol-assisted hybrid water electrolysis thus has been regarded as a promising alternative for hydrogen production concurrent with highly value-added conversion, which can avoid the harmful gas emissions and high pressure/temperature process involved in the industrial method [20].

In principle, the ethanol oxidation can follow the C1 and C2 reaction pathways. Based on a 4-electron transfer process in the C2 pathway, acetic acid (hence acetate) can be obtained from a partial oxidation of ethanol. The main use of acetic acid is as a raw material for vinyl acetate (about 33%) and acetic anhydride synthesis, and a solvent for purified terephthalic acid production [20,21]. In contrast, ethanol can also undergo complete oxidation via a 12-electron process in the C1 pathway to produce CO_2 , a major contributor to the greenhouse effect [22]. Considering both economic and environmental benefits, high selectivity for the electrooxidation of ethanol to generate acetic acid as a useful chemical product while minimizing the CO_2 side-product is required for the designed catalysts.

In terms of materials development, the state-of-the-art ethanol oxidation reaction (EOR) electrocatalysts are mainly based on noble metals, such as Pt, Pd, and Rh, due to their superior properties towards adsorption and dehydrogenation of ethanol [23,24]. However, noble metals can be easily poisoned by reaction intermediates such as carbon monoxide and methyl during the EOR process [22]. Moreover, the high cost and low scarcity of precious metals also limit their large-scale applications. Therefore, the design and exploitation of high-performance electrocatalysts based on earth-abundant metals for the EOR is urgent but still challenging. In this respect, transition-metal-based materials with inexpensive cost and anti-poisoning properties, such as metal alloys, oxides, and hydroxides, are promising electrocatalysts for the EOR in the alkaline media [25–27]. According to the Sabatier's principle, the ideal electrocatalyst should have neither too strong nor too weak adsorption properties towards surface-reactant interactions [28]. The synergistic effect between multi-metal active sites (e.g., Ni/Fe and Fe/Co) can enhance the intrinsic activity toward the OER and EOR, which can mainly be ascribed to the optimal binding energies to the reaction intermediates. For example, although Cu-based materials generally exhibit poor OER activity compared to Ni- or Co-based electrocatalysts, there is a report that doping Co into CuO can significantly improve OER performance [29]. Additionally, Wang et al. found that Cu-doped nickel oxyhydroxide can work as an efficient electrocatalyst toward the EOR, derived in part from the improved conductivity and formation of Ni^{3+} species [25]. However, given the competition within a wide potential range between the OER and EOR, it has been challenging to screen transition-metal-based catalyst materials with high selectivity for EOR. Moreover, there is a need to further improve the performance of non-noble metal-based EOR electrocatalysts to meet the requirements of large-scale applications.

In this work, we synthesize a nano-heterostructure containing CuO nanoarrays and NiOOH coupled with three-dimensional Cu foam (NiOOH-CuO/CF) via a facile strategy. Benefitting from the superior activity of two active species and a synergistic coupling effect between them, the nano-heterostructure exhibits remarkable alkaline EOR activity with a low potential of 1.347 V to deliver a current density of 200 mA cm^{-2} and a high conversion rate from ethanol into acetic acid, surpassing the reported state-of-the-art transition-metal-based EOR electrocatalysts. Density functional theory (DFT) calculations suggest that the localized charge density would be enhanced for a heterostructure containing CuO and NiOOH, and the interaction of the heterostructure support could reach ideal adsorption energy for the intermediate species of the EOR processes to reduce the reaction barrier. Additionally, the as-

assembled hybrid water electrolysis cell using NiOOH-CuO/CF enables concurrent conversion of ethanol into value-added acetic acid and renewable hydrogen production. This work provides new mechanistic insights and paves a route to design cost-effective and highly efficient transition metal compounds toward EOR electrocatalysis and related energy-saving H_2 production technology.

2. Experimental section

2.1. Preparation of Cu-based self-supported electrodes

A cleaned Cu foam ($1.0 \text{ cm} \times 1.0 \text{ cm}$) was first chemically etched at room temperature for 30 min by an ammonium persulfate aqueous solution, which contains 0.125 M ammonium persulfate solution and 2.5 M sodium hydroxide. After being taken out of the solution and washed with deionized water, the etched substrate ($\text{Cu}(\text{OH})_2/\text{CF}$) with a blue color was heated at 180°C for 1 h to obtain black CuO/CF. Finally, nickel oxyhydroxide was electrodeposited on CuO/CF at -1.08 V vs Ag/AgCl for 120 s in an electrolyte containing 0.15 M $\text{Ni}(\text{NO}_3)_2 \cdot 6 \text{H}_2\text{O}$ in water using a typical three-electrode electrochemical workstation. Pt wire and a saturated calomel electrode were used as the counter electrode and the reference electrode, respectively. For comparison, nickel oxyhydroxide on carbon cloth was also electrodeposited. The loading of nickel oxyhydroxide on CuO/CF and carbon cloth was $\approx 1.5 \text{ mg cm}^{-2}$.

2.2. Preparation of Pt/C/NF electrode

First, 10 mg of commercial Pt/C was dispersed in a mixture containing ethanol (1 mL) and 5 wt% Nafion (100 μL) solution, and the dispersion was sonicated for 1 h to obtain a homogeneous ink. Afterwards, 165 μL of the ink was dropped on Ni foam ($1.0 \text{ cm} \times 1.0 \text{ cm}$) and then dried at room temperature for further use.

2.3. Characterizations

The crystalline structures were analyzed by X-ray diffraction (Rigaku Ultima IV, Japan) with Cu $\text{K}\alpha$ radiation ($\lambda = 1.5418 \text{ \AA}$). The surface morphology and microstructure were analyzed by scanning electron microscopy (Hitachi S-4800) and high-resolution transmission electron microscopy (JEOL JEM-2200FS). X-ray photoelectron (K-alpha Thermo VG Scientific) spectroscopy measurements were performed to identify the elemental information on the surface.

2.4. Electrochemical measurements

All the electrochemical measurements were performed in a typical three-electrode system on an electrochemical workstation (Bio-logic VMP-300, France). The electrolyte was 1.0 M KOH for the OER and 1.0 M KOH and 1.0 M ethanol for the EOR and HER. The as-obtained self-supported electrodes were directly used as the working electrode, while a graphite rod and an Ag/AgCl electrode were used as the counter electrode and the reference electrode, respectively. The scanning rate for linear sweep voltammetry curves was maintained at 2 mV s^{-1} . Unless otherwise mentioned, all potentials were calibrated to a reversible hydrogen electrode utilizing the formula $E_{\text{RHE}} = E_{\text{Ag/AgCl}} + 0.197 + 0.059 \times \text{pH}$. Moreover, all potentials were compensated with 95%-iR correction according to the equation $E_{\text{corrected}} = E_{\text{uncorrected}} - 95\% \times iR$, where i and R are the current and internal resistance obtained by electrochemical impedance spectra (EIS). EIS were recorded with frequencies ranging from 10^5 to 10^{-1} Hz . The operational stability of the electrodes was evaluated by chronopotentiometric measurements.

Traditional water electrolysis and hybrid water electrolysis were evaluated using a two-electrode configuration by employing the NiOOH-CuO/CF electrode as the anode and the Pt/C/NF as the cathode. To characterize the liquid products of the EOR, the electrolyte after chronopotentiometric measurements was detected by ^1H nuclear magnetic

resonance (NMR, Bruker) with dimethylsulfoxide (DMSO) dissolved in D₂O as the internal standard and ¹³C NMR. The concentration of the liquid product was calculated by comparing the integral area of DMSO and the liquid products [25].

The detailed process of separation of acetate is as follows: (1) The main product of CH₃COONa in resulting mixture was transferred into CH₃COOH (acetate) by acidification treatment using hydrochloric acid (HCl) as an acidification reagent. (2) Subsequently, ethyl acetate, a good solvent for acetate, was added to above acidified solution. The new two-phase mixture was fully mixed in a separating funnel to extract acetate from water. Owing to the smaller density of ethyl acetate than water, acetate and ethyl acetate, as organic phase in upper layer, was collected for further purification. (3) Because of the lower boiling point of ethyl acetate than that of acetate, the acetate was successfully separated from organic phase by reduced pressure rotary evaporation.

2.5. Computational details

The present calculations employ the Vienna Ab initio Simulation Package (VASP) [30,31] implementation of DFT in conjunction with the projector augmented wave (PAW) formalism. The exchange-correlation term was modeled using the General Gradient Approximation (GGA) with Perdew-Burke-Ernzerhof (PBE) [32]. Consequently, the H 1s¹, O 2s²2p⁴, C 2s²2p², Ni 3d⁸4s², and Cu 3d¹⁰5s¹ states were treated as valence electrons. The electronic wave functions were expanded in plane waves using an energy cut-off of 500 eV. The Hubbard *U* model [33] was applied to describe the strong correlation of the localized Ni 3d and Cu 3d states, and the value of *U*_{eff} (= *U* − *J*) of Ni 3d and Cu 3d states was set to 6.40 eV and 7.00 eV, according to previous work [34,35]. Considering the magnetic nature of NiOOH, the spin polarization approach was employed in the present work. In addition, the DFT-D3 correction method in Grimme's scheme [36] was also used to accurately describe the long-range vdW interactions. The Monkhorst-Pack *k*-point meshes [37] were 4 × 4 × 1, and the force and energy convergence criteria were set to 0.02 eV/Å and 10^{−5} eV respectively, with a vacuum layer of 15 Å for lattice circulation to eliminate the interaction between two periodic images.

For CuO and NiOOH catalytic structures, we used a 1 × 1 primitive cell (lattice constants are *a* = *b* = *c* = 4.233 Å in CuO; *a* = *b* = 2.979 Å, *c* = 4.579 Å in NiOOH) to build periodic slab models with four Cu or four Ni sites per surface, with two layers at the bottom that were fixed during relaxation. The NiOOH-CuO heterointerface (IF) hybrid model was built in (2 × 2) CuO (111) and (2 × 2) NiOOH (001).

To maximize compliance with the structural characterization in experimental, the stable NiOOH-CuO heterointerface was supported on Cu (001) surface. Because the CuO and NiOOH surfaces may expose Cu, O, or Ni atoms, we constructed three possible interface structures and calculated the binding energy (*E*_b) in Fig. S19. The lowest *E*_b energy corresponds to the stable NiOOH-CuO heterointerface. *E*_b was defined as follows.

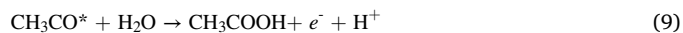
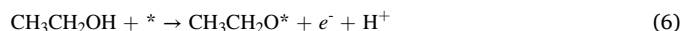
$$E_b = E_{(\text{NiOOH-CuO IF})} - E_{(\text{CuO})} - E_{(\text{NiOOH})} \quad (1)$$

For the Cu-supported NiOOH-CuO heterostructure (NiOOH-CuO/CF), the stable NiOOH-CuO IF hybrid was reduced on the Cu (001) surface consisting of 96 atoms. The optimized structures of the intermediates in the OER and EOR steps on the CuO of NiOOH-CuO/CF are shown in Fig. S15 and Fig. 4e.

The pathways of the OER are decomposed into the following elementary steps:



The pathways of the EOR are decomposed into the following elementary steps:



The reaction Gibbs free energy changes (ΔG) is defined as the difference between free energies of the final and initial states and is given by the formula:

$$\Delta G = \Delta E + \Delta \text{ZPE} - T\Delta S + \Delta G_U + \Delta G_{\text{pH}} \quad (10)$$

$$\Delta G_U = -neU \quad (11)$$

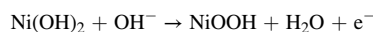
$$\Delta G_{\text{pH}} = -k_B T \ln[\text{H}^+] = \text{pH} \times k_B T \ln 10 \quad (12)$$

where *U* is the electrode applied potential, the energy differences ΔE are calculated reaction energy of reactant and product molecules adsorbed on substrates (at *U* = 0 and pH = 0). ΔZPE and ΔS are the change in zero-point energies and entropy due to the reaction.

3. Results and discussion

3.1. Synthesis and characterization of catalysts

In a typical experiment, NiOOH-CuO on three-dimensional Cu foam was constructed by a facile strategy, as schematically displayed in Fig. 1a. First, Cu(OH)₂ nanoarrays (denoted as Cu(OH)₂/CF) were in situ grown on commercial Cu foam through the chemical oxidation reaction and then calcined in the air to obtain CuO nanoarrays (denoted as CuO/CF), with the color of the materials changing from blue to black (see details in the **Experimental section**). Uniform one-dimensional (1D) nanowire morphologies of Cu(OH)₂ and CuO with an average of ≈ 5 μm length and ≈ 200 nm diameter were revealed by field emission scanning electron microscopy (FESEM) images (Figs. 1b–1d). These uniformly distributed nanowires are in situ formed from the three-dimensional substrate of CF with a smooth surface (Fig. S1). This unique nanoarray structure enables considerable exposure of active species on the surface and robust mechanical stability during the electrochemical reactions [12]. The phase transformation from Cu(OH)₂ to CuO was further confirmed by the corresponding X-ray diffraction (XRD) patterns (Fig. 1e) [13,38–40]. Subsequently, the nanosheet-like nickel hydroxide was electrodeposited on the surface of the CuO nanowires (Fig. 1f). No diffraction peak belonging to Ni was detected mainly due to the too strong peak from the CF and the low content of Ni species on the surface of the electrode (Fig. S2). High-resolution transmission electron microscopy (HRTEM) images verified the formation of a heterojunction, and the lattice fringes calculated as 0.29 and 0.25 nm correspond to the spacing of the (−202) and (111) planes of CuO and Ni(OH)₂, respectively (Fig. 1g) [41,42]. In addition, the homogeneous distribution of Cu, Ni, and O elements over the matrix is demonstrated by the elemental mapping images, indicating the uniformity of the heterostructure (Fig. 1h). X-ray photoelectron spectroscopy (XPS) was used to explore the elemental composition and surface valence states of transition metal ions. As shown in Fig. S3, the full spectrum demonstrates the presence of Cu, Ni, O, and C (for calibration) elements in the structure. The high-resolution XPS spectra of Ni 2p and Cu 2p suggest that Ni and Cu are present in the form of Ni²⁺ and Cu²⁺ oxidation states in the composites [13,43]. The above results demonstrate the successful fabrication of the nano-heterostructure by the proposed synthesis process. Considering the generally reported EOR reaction mechanism by Ni-based catalysts, the EOR reaction process by Ni(OH)₂ is as follows:



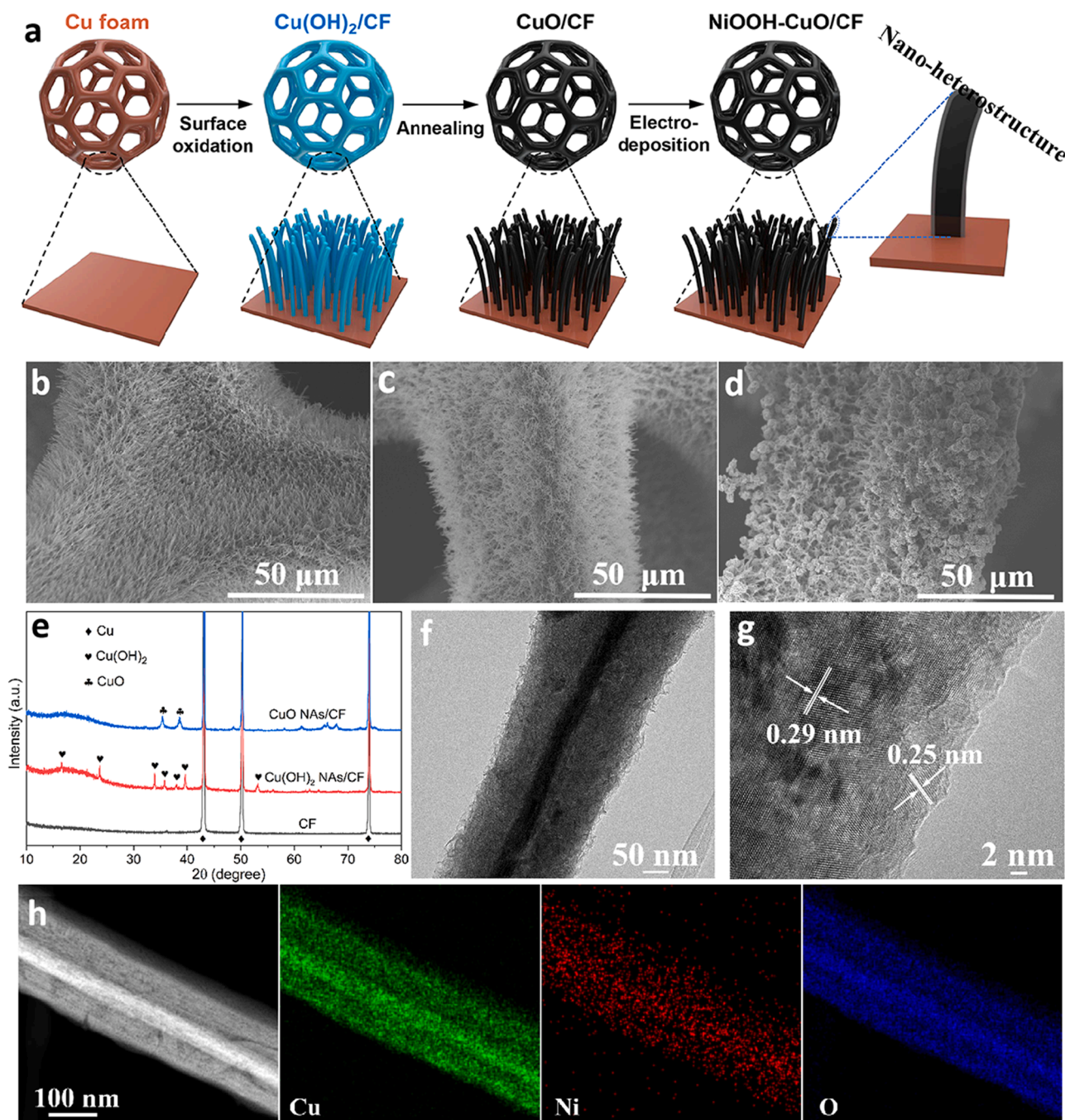
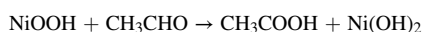
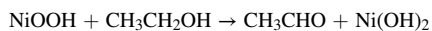


Fig. 1. Material synthesis and characterizations. (a) Schematic illustration of preparation of the nano-heterostructure in three steps: surface oxidation of Cu Foam to achieve $\text{Cu}(\text{OH})_2/\text{CF}$, annealing at 180°C to prepare CuO/CF , and electrodeposition process to obtain $\text{NiOOH-CuO}/\text{CF}$. SEM images of (b) $\text{Cu}(\text{OH})_2/\text{CF}$, (c) CuO/CF , and (d) $\text{NiOOH-CuO}/\text{CF}$. (e) XRD patterns of CF, $\text{Cu}(\text{OH})_2/\text{CF}$, and CuO/CF . (f) TEM image and (g) HRTEM image of $\text{NiOOH-CuO}/\text{CF}$. (h) HAADF-STEM image and the corresponding EDS mapping of Cu, Ni, and O elements.



The Ni-based catalysts inevitably undergo a self-oxidation process to generate the Ni^{3+} state NiOOH derivative on the surface providing direct active sites for the EOR [44–46]. Therefore, to better illustrate the actual active species during the electrochemical reactions, the electrodeposited $\text{Ni}(\text{OH})_2$ on CuO/CF and carbon cloth (CC) were first denoted as $\text{NiOOH-CuO}/\text{CF}$ and NiOOH/CC , respectively, which is the criterion for constructing the DFT calculation models (see details in the

Experimental section). In particular, CuO/CF and NiOOH/CC were used to confirm the high EOR activity of CuO and NiOOH by DFT calculations.

3.2. Electrocatalytic performance of designed electrodes

Electrochemical alkaline EOR and OER performance measurements were evaluated in 1.0 M KOH with and without a 1.0 M ethanol solution, respectively, at room temperature in a typical three-electrode system. The as-prepared self-supported electrodes were directly used as the working electrode. The high activity of CuO and NiOOH for the

EOR was confirmed by comparison with their OER activities. As shown in Fig. 2a, the potentials toward the OER to reach a current density of 50 mA cm^{-2} on CuO/CF and NiOOH/CC are 1.595 and 1.616 V vs RHE, respectively. However, with the existence of ethanol in the alkaline solutions, the potentials to deliver the same current density on CuO/CF and NiOOH/CC are reduced by 199 and 228 mV, respectively (Fig. 2b), suggesting that the electrooxidation of ethanol is more favorable than the OER over CuO and NiOOH. In addition, the EOR activities of bare CF, $\text{Cu}(\text{OH})_2/\text{CF}$, and bare CC were evaluated to further demonstrate the high EOR activities of CuO and NiOOH (Fig. S4). Moreover, the current density stabilized at 50 mA cm^{-2} over 30 h operation under the chronopotentiometry test for CuO/CF and NiOOH/CC, revealing satisfactory stability of these two active species (Fig. S5). Of note, the CuO/CF electrode exhibited higher current densities than that of the NiOOH/CC electrode at high potentials (e.g., 407.4 and 153.1 mA cm^{-2} for CuO/CF and NiOOH/CC, respectively, at 1.5 V vs RHE) (Fig. S6). This may be attributed to the in situ growth of the 1D nanowire structure of CuO with a high specific surface area that allows more active sites to be exposed during the electrochemical reaction. This highlights the crucial importance of constructing a 1D nanowire array on the 3D conductive metal foam (Fig. S7). The EOR performance of NiOOH-CuO/CF was further evaluated. Specifically, the NiOOH-CuO/CF shows reasonably good OER activity in 1.0 M KOH, reaching a current density of 200 mA cm^{-2} at

1.591 V vs RHE. This value significantly decreases to 1.347 vs RHE in 1.0 M KOH containing 1.0 M ethanol, also indicating that the EOR is more favorable than water oxidation on NiOOH-CuO/CF catalysts (Fig. 2c). Importantly, the potentials for the EOR decrease by at least 250 mV at the current densities of 250 and 350 mA cm^{-2} compared to the OER. Moreover, the peak at $\approx 1.39 \text{ V}$ for the OER curve is ascribed to the redox pair of $\text{Ni}^{2+}/\text{Ni}^{3+}$. The Tafel slope further illustrates that the EOR has a much smaller slope of 33.3 mV dec^{-1} than the OER ($155.4 \text{ mV dec}^{-1}$), indicating fast reaction kinetics of the EOR (Fig. S8). Fig. 2d shows a small onset potential of $\approx 1.32 \text{ V}$ vs RHE for NiOOH-CuO/CF toward the EOR, beyond which the current density increased obviously, and a current density of 200 mA cm^{-2} for the EOR is obtained at 1.347 V. When the current density reaches 200 mA cm^{-2} , the potential for the EOR of the NiOOH-CuO/CF decreased by 110 and 203 mV relative to those of CuO/CF and NiOOH/CC, respectively. Moreover, NiOOH-CuO/CF delivers the lowest Tafel slope of 33.3 mV dec^{-1} compared with CuO/CF (81.1 mV dec^{-1}) and NiOOH/CC (69.1 mV dec^{-1}), indicating remarkable improvement in the ethanol oxidation rates and reaction kinetics on the heterostructure (Fig. 2e). Corresponding electrochemical active surface area (ECSA) and electrochemical impedance spectroscopy (EIS) were also carried out to confirm the positive role of combining the two active species. The electrochemical double-layer capacitance (C_{dl}) was assessed via the CV method over a

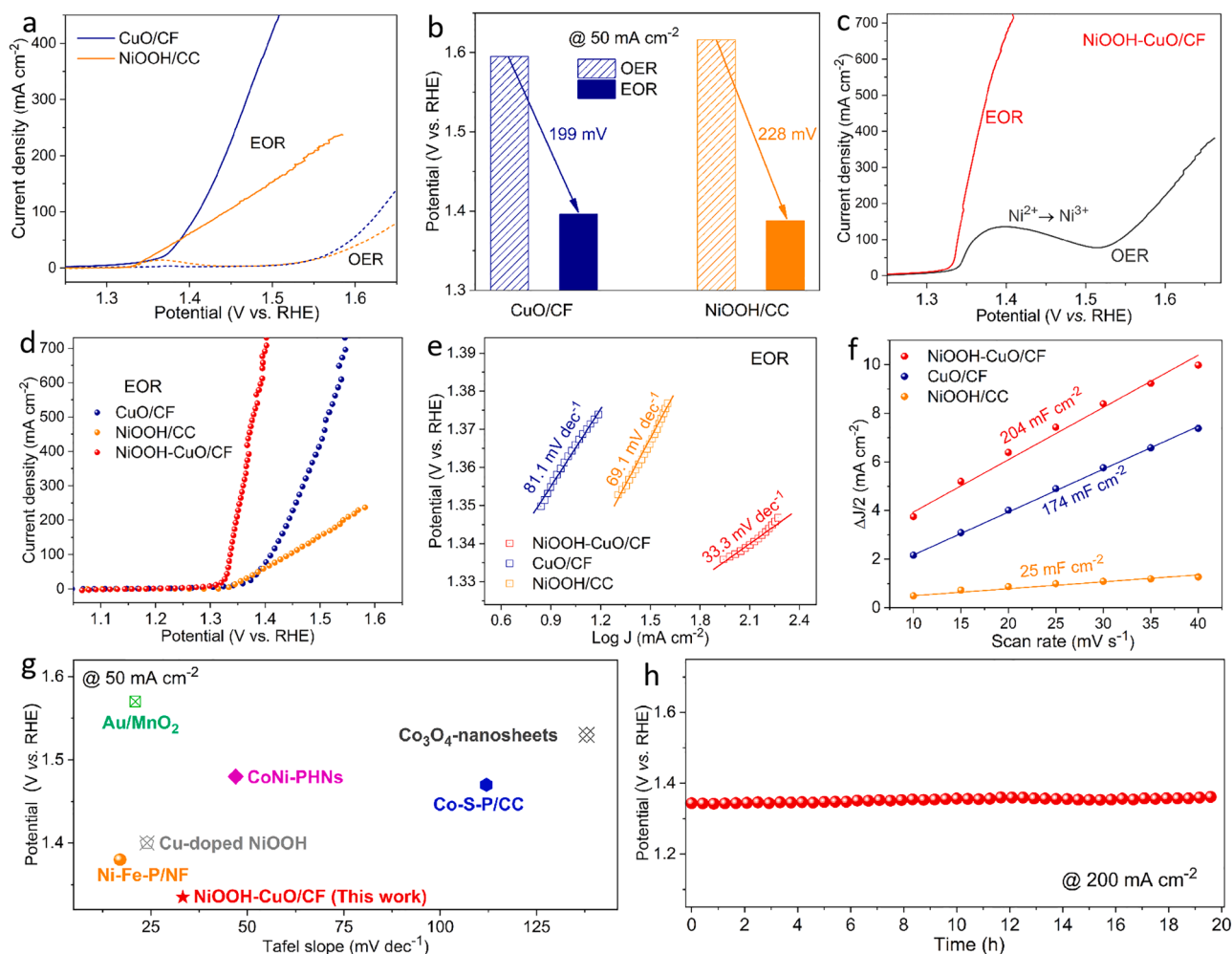


Fig. 2. EOR performance. (a) LSV curves of the CuO/CF and NiOOH/CC electrodes toward OER and EOR. (b) Potential comparisons of the CuO/CF and NiOOH/CC electrodes for OER and EOR at a current density of 50 mA cm^{-2} . (c) LSV curves of the NiOOH-CuO/CF electrode toward OER and EOR. (d) LSV curves of the CuO/CF, NiOOH/CC, and NiOOH-CuO/CF electrodes toward EOR. (e) Tafel plots of the CuO/CF, NiOOH/CC, and NiOOH-CuO/CF electrodes toward EOR derived from (d). (f) C_{dl} values of the CuO/CF, NiOOH/CC, and NiOOH-CuO/CF electrodes. (g) Tafel slope and potential at 50 mA cm^{-2} of NiOOH-CuO/CF and various recently reported transition-metal-based EOR electrocatalysts. (h) Chronopotentiometric curve at a fixed current density of 200 mA cm^{-2} .

non-faradaic potential range to evaluate ECSA (Fig. S9). The corresponding C_{dl} values of NiOOH-CuO/CF, CuO/CF, and NiOOH/CC were derived from CV curves obtained at different scan rates and found to be 204, 174, and 25 mF cm^{-2} , respectively, suggesting high exposure of efficient active sites to accelerate the EOR process in the NiOOH-CuO/CF heterojunction structure (Fig. 2f). The smallest value of charge transfer resistance obtained from NiOOH-CuO/CF further verifies the coupling effect between CuO and NiOOH for the enhanced EOR charge transfer kinetics (Fig. S10). The Tafel slope and potential at a current density of 50 mA cm^{-2} of NiOOH-CuO/CF are among the best levels achieved for transition-metal-based EOR electrocatalysts in alkaline solutions (Fig. 2g and Tab. S1). The durability of the optimal electrode in the EOR process was evaluated by the chronopotentiometry technique at a current density of 200 mA cm^{-2} , as illustrated in Fig. 2h. During the testing period, NiOOH-CuO/CF exhibits an almost constant potential (≈ 1.34 V), indicating good EOR operational stability. The catalytic activity after the durability testing is comparable to the initial state (Fig. S11). The morphology and composition of NiOOH-CuO/CF after chronopotentiometric testing were examined. The 1D nanoarray structure was well preserved with a small amount of aggregation after electrochemical testing (Fig. S12). Moreover, the surface crystalline structure of the nano-heterostructure electrode was also well preserved (Fig. S13), indicating that the nanostructure and composition were mostly maintained. Additionally, the high-resolution XPS spectra of Ni 2p and Cu 2p of CuO/CF, NiOOH/CC, and NiOOH-CuO/CF electrodes after EOR tests are almost identical to those of the pre-catalysts (Fig. S14). The above-mentioned results demonstrate that these nano-architectures are highly active and stable electrocatalysts toward the EOR in alkaline media.

3.3. Product detection

No apparent gas bubbles were generated on the NiOOH-CuO/CF electrode surface during the EOR process, indicating the possibility of

electrooxidation upgrading of ethanol into liquid products. To further probe the electrooxidation product, ^1H nuclear magnetic resonance (NMR) and ^{13}C NMR spectroscopy analyses were conducted on the electrolyte after ethanol oxidation electrolysis. First, to demonstrate the advantages of the individual active species and the hierarchical structure, the liquid products after 1000 CV cycling tests were analyzed. The chemical shift peaks at 1.06 and 3.54 ppm were ascribed to ethanol reactant in the electrolyte (Fig. 3a) [25]. The peak at 1.79 ppm was contributed by acetate, indicating that acetate was the main EOR product on the CuO/CF, NiOOH/CC, and NiOOH-CuO/CF electrodes (Fig. 3a) [25,47,48]. Acetate is the only organic oxidation product for NiOOH-CuO/CF, as further confirmed by ^{13}C NMR spectroscopy (Fig. 3b). Moreover, the hierarchical structure displayed higher acetate production, demonstrated by a qualitative comparison of the areas of the characteristic peaks [25]. The selectivity of the reaction was evaluated by Faradaic efficiency (FE). Comparing NMR results with theoretical values, the highest FE value (79.1%) of potassium acetate production from the electrooxidation of ethanol was achieved at a current density of 200 mA cm^{-2} (Fig. S15 and S16). To further evaluate the time-dependent ethanol-to-acetate conversion performance of the NiOOH-CuO/CF electrode, as shown in Fig. 3c, the conversion rate of acetate production from ethanol at different reaction times was evaluated (80 mL electrolyte). Good operational stability under a high current density of 200 mA cm^{-2} can be confirmed in Fig. 2h, which is a prerequisite for continuous acetate production. Notably, the conversion rates of acetate with the reaction times show a good linear relationship within 10 h ($R^2 = 0.9998$) (Fig. S17). To further check the linearity, a discontinuous (random) reaction time of 21 h was selected and the high correlation coefficient ($R^2 = 0.9997$) showed that the linear relationship is excellent (Figs. 3c and 3d). Again, ^{13}C NMR demonstrated that acetate is the only liquid product after chronopotentiometric testing of 21 h (Fig. 3e). The complete conversion of ethanol to acetate was confirmed by ^1H NMR for a reaction time of 45 h (Fig. S18), suggesting that superior yield and high selectivity of acetate production via ethanol electrooxidation can

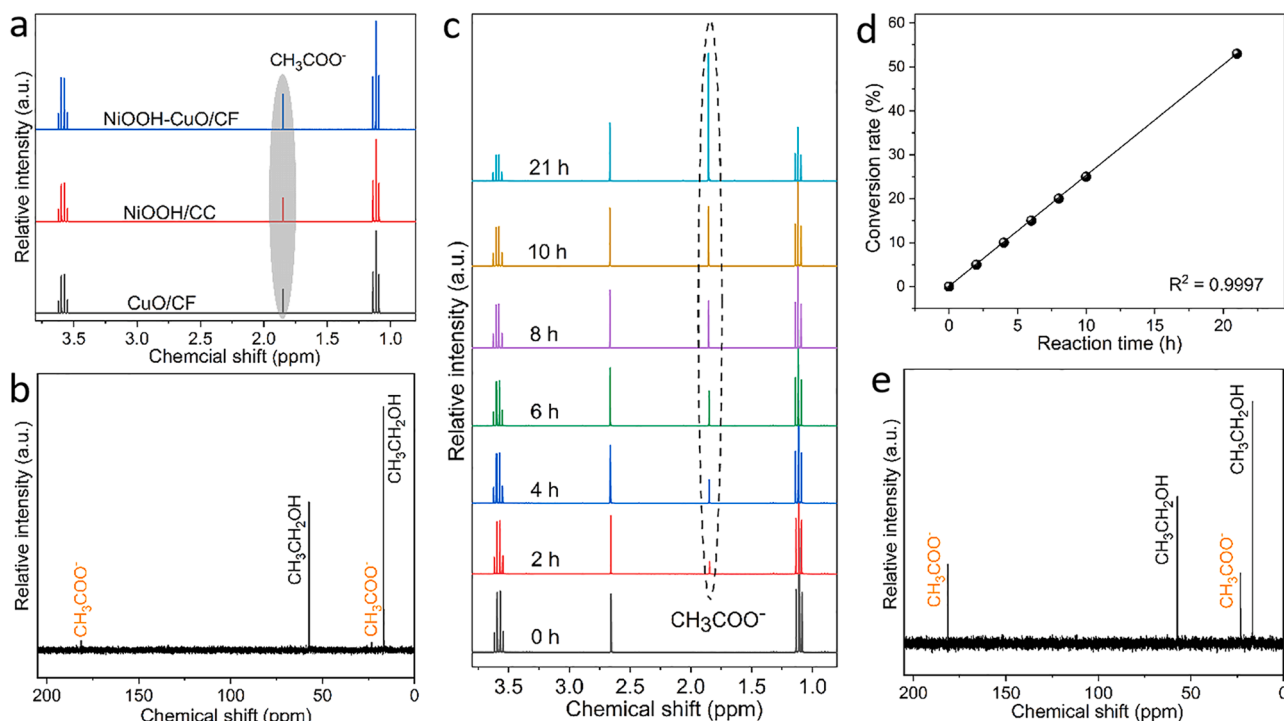


Fig. 3. Production identification and separation. (a) ^1H NMR spectra of liquid products after 1000 CV cycles on the CuO/CF, NiOOH, and NiOOH-CuO/CF electrodes. (b) ^{13}C NMR spectra of liquid products after 1000 CV cycles on the NiOOH-CuO/CF electrode. (c) ^1H NMR spectra of liquid products at different reaction times by chronopotentiometric measurement on the NiOOH-CuO/CF electrode. (d) Conversion rates of acetate at different reaction times in Fig. 3c. (e) ^{13}C NMR spectra of liquid products after chronopotentiometric testing of 21 h on the NiOOH-CuO/CF electrode.

be achieved by the nano-heterostructure.

3.4. Mechanism discussion

To explore the modification strategies on the low-cost electrocatalysts for promoting the EOR, the NiOOH-CuO heterostructure and the NiOOH-CuO heterostructure coupled with metallic Cu (NiOOH-CuO/CF) were investigated via theoretical calculations. Specifically, DFT was used to study the localized charge distribution on the model catalyst surfaces and to describe the OER and EOR electrocatalytic mechanisms by calculating the Gibbs free energy difference (ΔG). The ΔG is related to the adsorption energies of OH^* , O^* , OOH^* in OER steps, and $\text{CH}_3\text{CH}_2\text{OH}$, $\text{CH}_3\text{CH}_2\text{O}^*$, CH_3CHO^* , CH_3CO^* , CH_3COOH in EOR steps. To better fit the experimental real catalytic structure, we first screened the stable heterointerface between CuO and NiOOH (NiOOH-CuO IF), and then constructed the Cu-supported NiOOH-CuO heterostructure. As shown in Fig. S19, the chemical bonding interaction between Cu and O atoms at NiOOH-CuO IF has the lowest binding energy (E_b), indicating that the heterointerface is the most stable. The charge density difference diagram of the most stable NiOOH-CuO IF shown in Fig. 4a exhibits a significant increase in the localized charge density at the established heterointerface, indicating an interaction between CuO and NiOOH. Additionally, the Bader charge analysis of NiOOH-CuO IF

(Tab. S2) reveals that the Bader charge of a Cu atom at the interface between CuO and NiOOH ($+0.95|e|$) is larger than that of a pure CuO surface ($+0.83|e|$), and the Bader charge of Ni atom at the interface ($+1.15|e|$) is smaller than that of pure NiOOH surface ($+1.22|e|$). This indicates electron transfer from Cu to Ni atoms at the interface, and the high valence states of Cu atoms would be active sites. When the stable Cu-supported NiOOH-CuO IF is formed (Fig. 4b), the Bader data show a similar charge redistribution between Cu and Ni at the interface. Thus, the interaction between CuO and NiOOH by charge redistribution at the heterointerface might modulate the OER and EOR processes into an energetically more favorable pathway.

Based on the above results, we further examined the ΔG of the OER and the EOR procedure on a pure CuO (111) surface, pure NiOOH (001) surface, CuO at NiOOH-CuO heterointerface (IF-CuO), and NiOOH at NiOOH-CuO heterointerface (IF-NiOOH). Here, the metal-site adsorbate evolution mechanism was considered as the reaction mechanism involving proton-electron transfer steps [34,48,49]. As shown in Fig. 4c, the rate-limiting ΔG of the OER processes in IF-CuO and IF-NiOOH are 2.05 and 2.55 eV, respectively, which are lower than that for the pure CuO surface (2.42 eV) and NiOOH (2.63 eV) surface. This DFT calculation demonstrated that the NiOOH-CuO interface working as OER active sites in NiOOH-CuO/CF IF can be synergistically enhanced through the interaction between CuO and NiOOH (Fig. S20).

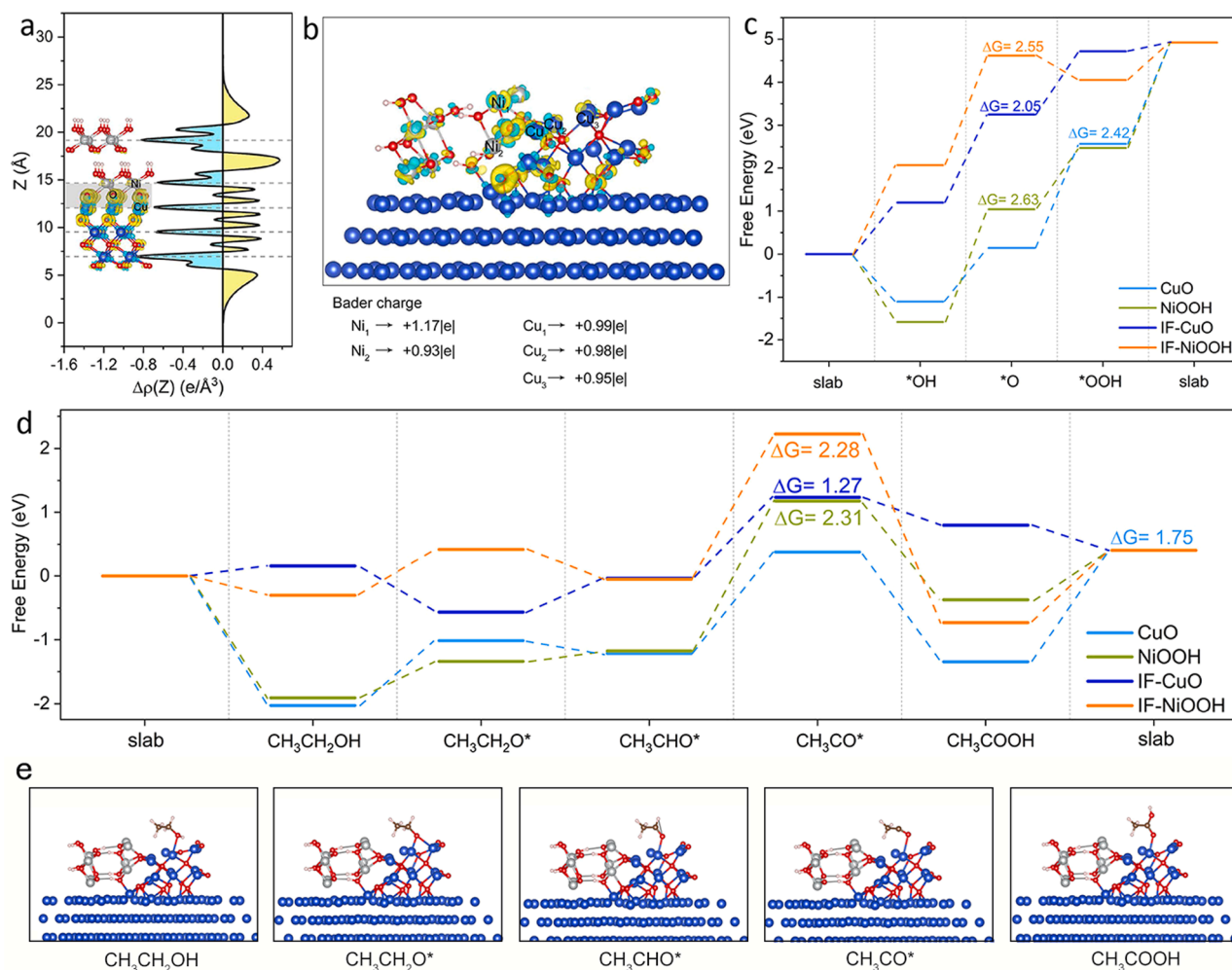


Fig. 4. Atomic models with the charge density difference of catalyst surfaces, as well as OER and EOR mechanisms. (a) Plane-integrated electron density differences along the vertical direction. The inset shows the charge density difference of the Cu-supported NiOOH-CuO IF (NiOOH-CuO/CF). (b) The charge density difference of the Cu-supported NiOOH-CuO IF (NiOOH-CuO/CF). (c, d) The free energies diagram of OER and EOR steps on pure CuO surfaces, pure NiOOH surfaces, CuO at the interface of NiOOH-CuO/CF (IF-CuO), and NiOOH at the interface of NiOOH-CuO/CF (IF-NiOOH). (e) The optimized structures of the intermediates in EOR on the IF-CuO.

Meanwhile, we show the EOR electrocatalytic mechanism in Figs. 4d and 4e. From the free energies diagram of EOR steps, it can be observed that the reaction procedure of the initial three processes of ethanol dehydrogenation ($\text{CH}_3\text{CH}_2\text{OH}$, $\text{CH}_3\text{CH}_2\text{O}^*$, and CH_3CHO^* states) over IF-CuO and IF-NiOOH sites is easier than that over pure CuO and NiOOH sites, because of the absolute value of ΔG near to the thermal neutral position (0). Moreover, compared to the rate-determining steps of pure

CuO and NiOOH sites, the energy of $\text{CH}_3\text{CHO}^* \rightarrow \text{CH}_3\text{CO}^*$ step of IF-CuO and IF-NiOOH slumps and further greatly facilitates the reaction. Thermodynamically, the ΔG of the rate-determining steps for the EOR reaction on IF-CuO and IF-NiOOH is lower than that of the OER, indicating that the EOR occurs preferentially when the NiOOH-CuO interface may experience both EOR and OER reactions. In this Cu-supported heterojunction, IF-CuO has the best EOR performance, with the lowest

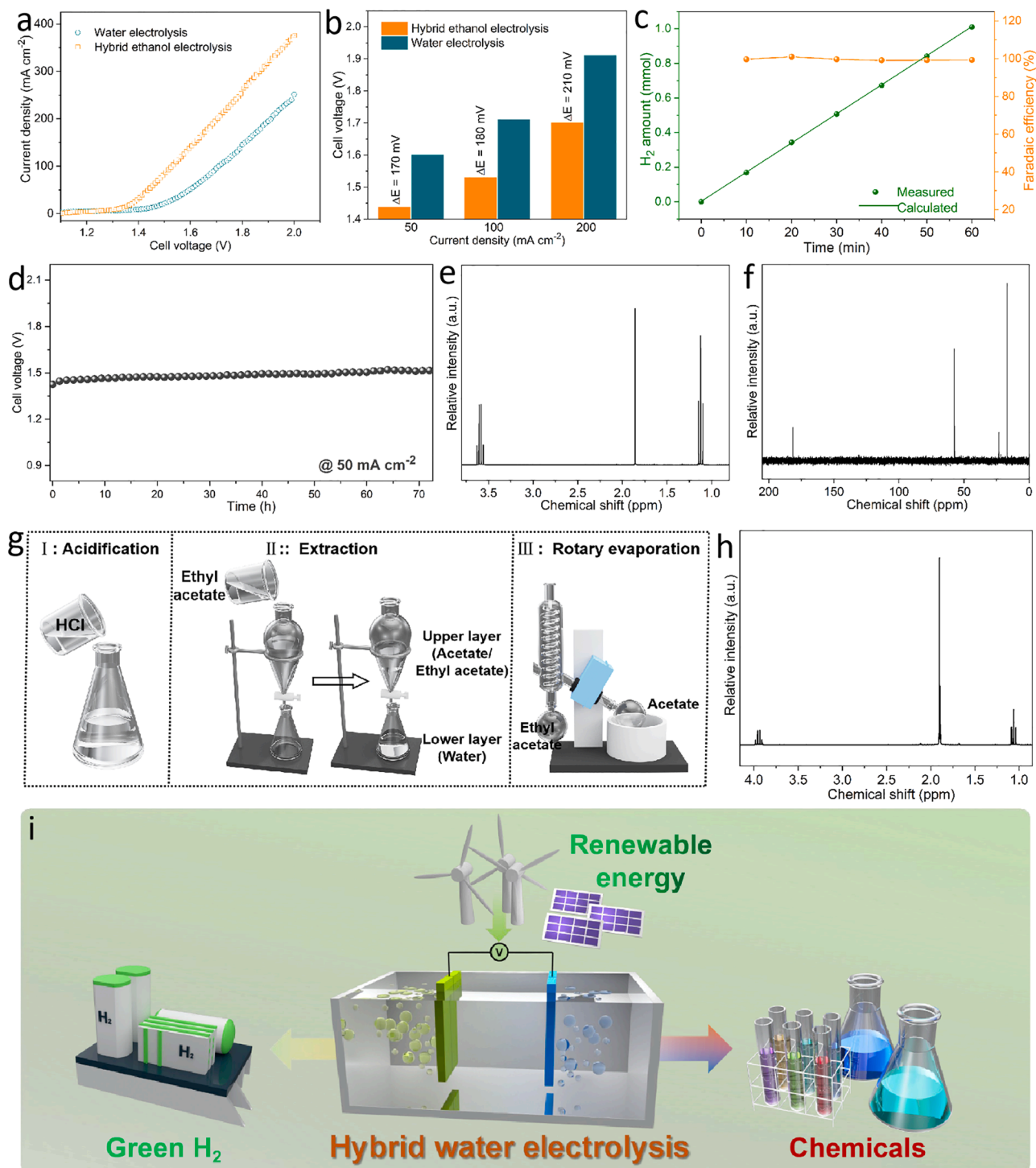


Fig. 5. Hybrid ethanol electrolysis performance. (a) Polarization curves electrodes in HER//OER and HER//EOR coupled systems. (b) Comparison of cell voltages for water electrolysis and hybrid ethanol electrolysis at different current densities. (c) Faradaic efficiency of H₂ production in hybrid ethanol electrolysis upon operation time. (d) Chronopotentiometry curve of the hybrid ethanol electrolyser. (e) ¹H and (f) ¹³C NMR spectra of the electrolyte after stability test. (g) Schematic illustration of the liquid production separation. (h) ¹H NMR analysis of the separated acetate. (i) Schematic illustration for the advantages of hybrid water electrolysis, including usage of renewable energy as powder source and generations of green hydrogen at the cathode and high-value chemicals at the anode.

energy barrier at the rate-limiting step. The excellent activity of the IF-CuO, on the one hand, originates from the charge transport of the interfacial neighbor NiOOH, which further reduces the energy barrier. In addition, due to the strong electrical conductivity of Cu as the support, the EOR performance of the IF-CuO can also be enhanced by improving electron transport. The above calculation of catalytic performance ignores the solution effect. Although the solution effect can reflect the dynamic structure occurring at the solid-liquid interface, it has little effect on the coupling of the heterojunction structure. To sum up, the coupling between CuO and NiOOH by charge redistribution upon the interface is critical, synergistically accelerating the EOR process into an energetically more favorable pathway and highlighting the importance of 3D conductive foam as the substrate.

3.5. Evaluation of electrocatalytic activity for ethanol electrolysis

To demonstrate the applicability of the NiOOH-CuO/CF catalyst for hybrid water electrolysis with integrated ethanol oxidation, a two-electrode electrolyzer was constructed by employing the NiOOH-CuO/CF electrode as the anode and Pt/C/NF as the cathode (Fig. S21). For comparison, a conventional alkaline electrolysis cell was also assembled using 1.0 M KOH as the electrolyte. Fig. 5a depicts the polarization curves of the electrolyzer cells conducted in the electrolyte with or without ethanol. The traditional alkaline electrolyzer requires a cell voltage of 1.611 V to deliver an electrolytic current density of 50 mA cm⁻². As expected, with the addition of 1.0 M ethanol into the alkaline electrolyte, there was a remarkable decrease in the applied voltage (1.430 V) to reach the same current density. Fig. 5b compares the applied voltage required for current densities of 50, 100, and 200 mA cm⁻² between the conventional and hybrid water electrolyzer, and the latter achieves a remarkable decrease of at least 170 mV in applied voltage. The Faradaic efficiency of the Pt/C/NF electrode for H₂ production was also tested [50]. The measured quantity of H₂ was close to the theoretically predicted value, and thus the calculated FE was close to 100% (Fig. 5c). Additionally, no obvious activity degradation was observed after evaluation by the chronopotentiometry technique at a fixed current density of 50 mA cm⁻² for 70 h, revealing good stability of this electrolyzer (Fig. 5d). Apart from the production of hydrogen, the products at the anode production were identified by NMR and acetic acid is the only liquid product, as confirmed by ¹H and ¹³C NMR (Figs. 5e and 5f).

With the impressive acetate yield of the NiOOH-CuO/CF electrocatalyst, we further demonstrated acetate separation from the aqueous electrolyte after the EOR process (Fig. 5g). The aqueous electrolyte was first treated by acidification with 6.0 M hydrochloric acid to adjust the pH value to 1–2, which realizes the transformation of potassium acetate to acetic acid. The separation of acetate from the resulting mixture was then conducted by extraction with ethyl acetate. Due to the difference in the boiling point between ethyl acetate (77.2 °C) and acetate (117.9 °C), ethyl acetate can be removed by a distillation technique (Fig. 5h). Overall, we demonstrated a complete process that converts biomass (ethanol) into a high-value chemical (acetate). Moreover, this is the first report that directly separates the organic product from the aqueous solutions for EOR electrocatalysis, which also provides a potential approach for the mass production of high-value chemicals. Therefore, the tradition metal-based electrode presented in this study clearly suggests that it is a promising material technology that enables hybrid water electrolysis to use renewable energy as the power source for the generations of green hydrogen at the cathode and high-value chemicals at the anode (Fig. 5i).

4. Conclusions

We succeeded in developing a high-performance nano-heterostructure electrode toward ethanol oxidation for hybrid water electrolysis. The developed NiOOH-CuO/CF electrode is composed only of

cheap 3d transition metals and is easy to manufacture over a large area. Notably, the synergistic coupling between the interface-rich NiOOH-CuO with metallic Cu significantly modulates the charge density and the electronic structure at the interface, achieving ideal adsorption energy and a reduced energy barrier for EOR intermediates, and ultimately boosting the EOR activity. As a result, the experimental analysis confirmed the high EOR performance of the NiOOH-CuO/CF electrode, characterized by a low potential of 1.347 V to drive a current density of 200 mA cm⁻², excellent operational stability, and high selectivity toward the EOR. Additionally, hybrid water electrolysis also demonstrated exceptional performance with energy-saving H₂ production and oxidation of ethanol into acetic acid. More importantly, we first propose a complete process that combined with acidification and extraction processes to realize the separation of organic products from the aqueous electrolyte, which suggests a practical approach to convert biomass into valuable products by the electrocatalysis method.

CRedit authorship contribution statement

Hainan Sun: Conceptualization, Methodology, Writing – original draft. **Lili Li:** Conceptualization, Writing – review & editing. **Yahui Chen:** Validation, Methodology, Investigation. **Hyunseung Kim:** Investigation. **Xiaomin Xu:** Formal analysis. **Daqin Guan:** Formal analysis. **Zhiwei Hu:** Investigation. **Linjuan Zhang:** Supervision, Project administration, Review & editing. **Zongping Shao:** Supervision, Project administration, Review & editing. **WooChul Jung:** Supervision, Project administration, Funding acquisition, Review & editing.

Declaration of Competing Interest

The authors declare that they have no known competing financial interests or personal relationships that could have appeared to influence the work reported in this paper.

Data availability

Data will be made available on request.

Acknowledgements

H.S., L.L. and Y.C. contributed equally to this work. This research was supported by National R&D Program through the National Research Foundation of Korea (NRF), grant number 2020M3H4A3105826 and 2022M3H4A1A04085313.

Appendix A. Supporting information

Supplementary data associated with this article can be found in the online version at doi:10.1016/j.apcatb.2023.122388.

References

- [1] M.F. Lagadec, A. Grimaud, Water electrolysis with closed and open electrochemical systems, *Nat. Mater.* 19 (2020) 1140–1150, <https://doi.org/10.1038/s41563-020-0788-3>.
- [2] Z.W. Seh, J. Kibsgaard, C.F. Dickens, I. Chorkendorff, J.K. Nørskov, T.F. Jaramillo, Combining theory and experiment in electrocatalysis: insights into materials design, *Science* 355 (2017) eaad4998, <https://doi.org/10.1126/science.aad4998>.
- [3] H. Sun, X. Xu, H. Kim, W. Jung, W. Zhou, Z. Shao, Electrochemical water splitting: bridging the gaps between fundamental research and industrial applications, *Energy Environ. Mater.* (2022), e12441, <https://doi.org/10.1002/eeem.2.12441>.
- [4] H.C. Fu, X.H. Wang, X.H. Chen, Q. Zhang, N.B. Li, H.Q. Luo, Interfacial engineering of Ni(OH)₂ on W₂C for remarkable alkaline hydrogen production, *Appl. Catal. B Environ.* 301 (2022), 120818, <https://doi.org/10.1016/j.apcatb.2021.120818>.
- [5] X. Xu, Z. Shao, S.P. Jiang, High-entropy materials for water electrolysis, *Energy Technol.* 10 (2022) 2200573, <https://doi.org/10.1002/ente.202200573>.
- [6] H. Sun, X. Xu, Y. Song, W. Zhou, Z. Shao, Designing high-valence metal sites for electrochemical water splitting, *Adv. Funct. Mater.* 31 (2021) 2009779, <https://doi.org/10.1002/adfm.202009779>.

- [7] S. Kim, J.-W. Jung, D. Song, S.-H. Cho, J. Kim, J.K. Kim, D. Oh, H. Sun, E. Cho, I.-D. Kim, W. Jung, Exceptionally durable Co-Fe-exsolved $\text{Sr}_{0.95}\text{Nb}_{0.1}\text{Co}_{0.7}\text{Fe}_{0.2}\text{O}_{3-\delta}$ catalyst for rechargeable Zn–air batteries, *Appl. Catal. B Environ.* 315 (2022), 121553, <https://doi.org/10.1016/j.apcatb.2022.121553>.
- [8] Z.-F. Huang, J. Song, S. Dou, X. Li, J. Wang, X. Wang, Strategies to break the scaling relation toward enhanced oxygen electrocatalysis, *Matter* 1 (2019) 1494–1518, <https://doi.org/10.1016/j.matt.2019.09.011>.
- [9] H. Sun, W. Jung, Recent advances in doped ruthenium oxides as high-efficiency electrocatalysts for the oxygen evolution reaction, *J. Mater. Chem. A* 9 (2021) 15506–15521, <https://doi.org/10.1039/D1TA03452A>.
- [10] K.S. Exner, Why the breaking of the OOH versus OH scaling relation might cause decreased electrocatalytic activity, *Chem. Catal.* 1 (2021) 258–271, <https://doi.org/10.1016/j.checat.2021.06.011>.
- [11] C. Deng, C.Y. Toe, X. Li, J. Tan, H. Yang, Q. Hu, C. He, Earth-abundant metal-based electrocatalysts promoted anodic reaction in hybrid water electrolysis for efficient hydrogen production: recent progress and perspectives, *Adv. Energy Mater.* 12 (2022) 2201047, <https://doi.org/10.1002/aenm.202201047>.
- [12] H. Sun, H. Kim, S. Song, W. Jung, Copper foam-derived electrodes as efficient electrocatalysts for conventional and hybrid water electrolysis, *Mater. Rep. Energy* 2 (2022), 100092, <https://doi.org/10.1016/j.matre.2022.100092>.
- [13] H. Sun, J. Liu, G. Chen, H. Kim, S. Kim, Z. Hu, J.-M. Chen, S.-C. Haw, F. Ciucci, W. Jung, Hierarchical structure of CuO nanowires decorated with $\text{Ni}(\text{OH})_2$ supported on Cu foam for hydrogen production via urea electrocatalysis, *Small Methods* 6 (2022) 2101017, <https://doi.org/10.1002/smt.202101017>.
- [14] S.-K. Geng, Y. Zheng, S.-Q. Li, H. Su, X. Zhao, J. Hu, H.-B. Shu, M. Jaroniec, P. Chen, Q.-H. Liu, S.-Z. Qiao, Nickel ferrocyanide as a high-performance urea electrocatalyst, *Nat. Energy* 6 (2021) 904–912, <https://doi.org/10.1038/s41560-021-00899-2>.
- [15] L. Fan, Y. Ji, G. Wang, J. Chen, K. Chen, X. Liu, Z. Wen, High entropy alloy electrocatalytic electrode toward alkaline glycerol valorization coupling with acidic hydrogen production, *J. Am. Chem. Soc.* 144 (2022) 7224–7235, <https://doi.org/10.1021/jacs.1c13740>.
- [16] Q. Xue, X.-Y. Bai, Y. Zhao, Y.-N. Li, T.-J. Wang, H.-Y. Sun, F.-M. Li, P. Chen, P. Jin, S.-B. Yin, Y. Chen, Au core-PtAu alloy shell nanowires for formic acid electrolysis, *J. Energy Chem.* 65 (2022) 94–102, <https://doi.org/10.1016/j.jechem.2021.05.034>.
- [17] S. He, Y. Liu, H. Li, Q. Wu, D. Ma, D. Gao, J. Bi, Y. Yang, C. Cui, Highly dispersed Mo sites on Pd nanosheets enable selective ethanol-to-acetate conversion, *ACS Appl. Mater. Interfaces* 13 (2021) 13311–13318, <https://doi.org/10.1021/acsami.1c01010>.
- [18] R.A. Dagle, A.D. Winkelman, K.K. Ramasamy, V. Lebarbier Dagle, R.S. Weber, Ethanol as a renewable building block for fuels and chemicals, *Ind. Eng. Chem. Res.* 59 (2020) 4843–4853, <https://doi.org/10.1021/acs.iecr.9b05729>.
- [19] G. Liu, G. Yang, X. Peng, J. Wu, N. Tsubaki, Recent advances in the routes and catalysts for ethanol synthesis from syngas, *Chem. Soc. Rev.* 51 (2022) 5606–5659, <https://doi.org/10.1039/D0CS01003K>.
- [20] P. Kalck, C. Le Berre, P. Serp, Recent advances in the methanol carbonylation reaction into acetic acid, *Coord. Chem. Rev.* 402 (2020), 213078, <https://doi.org/10.1016/j.ccr.2019.1213078>.
- [21] A.C. Dimian, A.A. Kiss, Enhancing the separation efficiency in acetic acid manufacturing by methanol carbonylation, *Chem. Eng. Technol.* 44 (2021) 1792–1802, <https://doi.org/10.1002/ceat.202100230>.
- [22] S. Bai, Y. Xu, K. Cao, X. Huang, Selective ethanol oxidation reaction at the Rh–SnO₂ interface, *Adv. Mater.* 33 (2021) 2005767, <https://doi.org/10.1002/adma.202005767>.
- [23] T.-J. Wang, H.-Y. Sun, Q. Xue, M.-J. Zhong, F.-M. Li, X. Tian, P. Chen, S.-B.I. Yin, Y. Chen, Holey platinum nanotubes for ethanol electrochemical reforming in aqueous solution, *Sci. Bull.* 66 (2021) 2079–2089, <https://doi.org/10.1016/j.scib.2021.05.027>.
- [24] S. Zhang, S.E. Saji, Z. Yin, H. Zhang, Y. Du, C.-H. Yan, Rare-earth incorporated alloy catalysts: synthesis, properties, and applications, *Adv. Mater.* 33 (2021) 2005988, <https://doi.org/10.1002/adma.202005988>.
- [25] H. Wang, A. Guan, J. Zhang, Y. Mi, S. Li, T. Yuan, C. Jing, L. Zhang, L. Zhang, G. Zheng, Copper-doped nickel oxyhydroxide for efficient electrocatalytic ethanol oxidation, *Chin. J. Catal.* 43 (2022) 1478–1484, [https://doi.org/10.1016/S1872-2067\(21\)63995-5](https://doi.org/10.1016/S1872-2067(21)63995-5).
- [26] J. Li, X. Wang, C. Xing, L. Li, S. Mu, X. Han, R. He, Z. Liang, P. Martinez, Y. Yi, Q. Wu, H. Pan, J. Arbiol, C. Cui, Y. Zhang, A. Cabot, Electrochemical reforming of ethanol with acetate Co-Production on nickel cobalt selenide nanoparticles, *Chem. Eng. J.* 440 (2022), 135817, <https://doi.org/10.1016/j.cej.2022.135817>.
- [27] S. Sheng, Y. Song, L. Sha, K. Ye, K. Zhu, Y. Gao, J. Yan, G. Wang, D. Cao, Simultaneous hydrogen evolution and ethanol oxidation in alkaline medium via a self-supported bifunctional electrocatalyst of Ni-Fe phosphide/Ni foam, *Appl. Surf. Sci.* 561 (2021), 150080, <https://doi.org/10.1016/j.apsusc.2021.150080>.
- [28] Y. Pan, X. Xu, Y. Zhong, L. Ge, Y. Chen, J.-P.M. Veder, D. Guan, R. O'Hayre, M. Li, G. Wang, H. Wang, W. Zhou, Z. Shao, Direct evidence of boosted oxygen evolution over perovskite by enhanced lattice oxygen participation, *Nat. Commun.* 11 (2020), 2002.
- [29] X. Xiong, C. You, Z. Liu, A.M. Asiri, X. Sun, Co-doped CuO nanoarray: an efficient oxygen evolution reaction electrocatalyst with enhanced activity, *ACS Sustain. Chem. Eng.* 6 (2018) 2883–2887, <https://doi.org/10.1038/s41467-020-15873-x>.
- [30] G. Kresse, J. Furthmüller, Efficient iterative schemes for ab initio total-energy calculations using a plane-wave basis set, *Phys. Rev. B* 54 (1996) 11169–11186, <https://doi.org/10.1103/PhysRevB.54.11169>.
- [31] G. Kresse, D. Joubert, From ultrasoft pseudopotentials to the projector augmented-wave method, *Phys. Rev. B* 59 (1999) 1758–1775, <https://doi.org/10.1103/PhysRevB.59.1758>.
- [32] J.P. Perdew, K. Burke, M. Ernzerhof, Generalized gradient approximation made simple, *Phys. Rev. Lett.* 77 (1996) 3865–3868, <https://doi.org/10.1103/PhysRevLett.77.3865>.
- [33] S.L. Dudarev, G.A. Botton, S.Y. Savrasov, C.J. Humphreys, A.P. Sutton, Electron-energy-loss spectra and the structural stability of nickel oxide: an LSDA+U study, *Phys. Rev. B* 57 (1998) 1505–1509, <https://doi.org/10.1103/PhysRevB.57.1505>.
- [34] W. Niu, J. Shi, L. Ju, Z. Li, N. Orlovskaya, Y. Liu, Y. Yang, Understanding synergism of cobalt metal and copper oxide toward highly efficient electrocatalytic oxygen evolution, *ACS Catal.* 8 (2018) 12030–12040, <https://doi.org/10.1021/acscatal.8b03702>.
- [35] X. Ren, C. Wei, Y. Sun, X. Liu, F. Meng, X. Meng, S. Sun, S. Xi, Y. Du, Z. Bi, G. Shang, A.C. Fisher, L. Gu, Z.J. Xu, Constructing an adaptive heterojunction as a highly active catalyst for the oxygen evolution reaction, *Adv. Mater.* 32 (2020) 2001292, <https://doi.org/10.1002/adma.202001292>.
- [36] S. Grimme, S. Ehrlich, L. Goerigk, Effect of the damping function in dispersion corrected density functional theory, *J. Comput. Chem.* 32 (2011) 1456–1465, <https://doi.org/10.1002/jcc.21759>.
- [37] H.J. Monkhorst, J.D. Pack, Special points for Brillouin-zone integrations, *Phys. Rev. B* 13 (1976) 5188–5192, <https://doi.org/10.1103/PhysRevB.13.5188>.
- [38] J. Hu, A. Al-Salihi, J. Wang, X. Li, Y. Fu, Z. Li, X. Han, B. Song, P. Xu, Improved interface charge transfer and redistribution in CuO-CoOOH p-n heterojunction nanoarray electrocatalyst for enhanced oxygen evolution reaction, *Adv. Sci.* 8 (2021) 2103314, <https://doi.org/10.1002/adv.202103314>.
- [39] L. Tabassum, H. Tasnim, S. Shubhashish, I. Perera, T. Bhosale, M. Li, S. March, M. K. Islam, S.L. Suib, Selenium-doped copper oxide nanoarrays: robust electrocatalyst for the oxygen evolution reaction with ultralow overpotential, *Appl. Mater. Today* 27 (2022), 101485, <https://doi.org/10.1016/j.apmt.2022.101485>.
- [40] A. Kumar, V.Q. Bui, J. Lee, A.R. Jadhav, Y. Hwang, M.G. Kim, Y. Kawazoe, H. Lee, Modulating interfacial charge density of $\text{NiP}_2\text{-FeP}_2$ via coupling with metallic Cu for accelerating alkaline hydrogen evolution, *ACS Energy Lett.* 6 (2021) 354–363, <https://doi.org/10.1021/acseenergylett.0c02498>.
- [41] S. Li, W. Huang, Y. Yang, J. Ulstrup, L. Ci, J. Zhang, J. Lou, P. Si, Hierarchical layer-by-layer porous $\text{FeCo}_2\text{S}_4\text{@Ni}(\text{OH})_2$ arrays for all-solid-state asymmetric supercapacitors, *J. Mater. Chem. A* 6 (2018) 20480–20490, <https://doi.org/10.1039/C8TA07598K>.
- [42] R. Rawat, A. Tiwari, N. Arun, S.V.S.N. Rao, A.P. Pathak, A. Tripathi, Solvents effect on the morphology and stability of Cu/CuO nanoparticles synthesized at high fluence laser ablation, *ChemistrySelect* 4 (2019) 10471–10482, <https://doi.org/10.1002/slct.201902344>.
- [43] L. Yu, H. Zhou, J. Sun, F. Qin, F. Yu, J. Bao, Y. Yu, S. Chen, Z. Ren, Cu nanowires shelled with NiFe layered double hydroxide nanosheets as bifunctional electrocatalysts for overall water splitting, *Energy Environ. Sci.* 10 (2017) 1820–1827, <https://doi.org/10.1039/C7EE01571B>.
- [44] L. Xu, Z. Wang, X. Chen, Z. Qu, F. Li, W. Yang, Ultrathin layered double hydroxide nanosheets with Ni(III) active species obtained by exfoliation for highly efficient ethanol electrooxidation, *Electrochim. Acta* 260 (2018) 898–904, <https://doi.org/10.1016/j.electacta.2017.12.065>.
- [45] L. Yaquob, T. Noor, N. Iqbal, A comprehensive and critical review of the recent progress in electrocatalysts for the ethanol oxidation reaction, *RSC Adv.* 11 (2021) 16768–16804, <https://doi.org/10.1039/D1RA01841H>.
- [46] W. Chen, C. Xie, Y. Wang, Y. Zou, C.-L. Dong, Y.-C. Huang, Z. Xiao, Z. Wei, S. Du, C. Chen, B. Zhou, J. Ma, S. Wang, Activity origins and design principles of nickel-based catalysts for nucleophilic electrooxidation, *Chem* 6 (2020) 2974–2993, <https://doi.org/10.1016/j.chempr.2020.07.022>.
- [47] W. Wang, Y.-B. Zhu, Q. Wen, Y. Wang, J. Xia, C. Li, M.-W. Chen, Y. Liu, H. Li, H.-A. Wu, T. Zhai, Modulation of molecular spatial distribution and chemisorption with perforated nanosheets for ethanol electro-oxidation, *Adv. Mater.* 31 (2019) 1900528, <https://doi.org/10.1002/adma.201900528>.
- [48] Y. Zhu, X. Zhu, L. Bu, Q. Shao, Y. Li, Z. Hu, C.-T. Chen, C.-W. Pao, S. Yang, X. Huang, Single-atom in-doped subnanometer Pt nanowires for simultaneous hydrogen generation and biomass upgrading, *Adv. Funct. Mater.* 30 (2020) 2004310, <https://doi.org/10.1002/adfm.202004310>.
- [49] A. Govind Rajan, J.M.P. Martinez, E.A. Carter, Facet-independent oxygen evolution activity of pure $\beta\text{-NiOOH}$: different chemistries leading to similar overpotentials, *J. Am. Chem. Soc.* 142 (2020) 3600–3612, <https://doi.org/10.1021/jacs.9b13708>.
- [50] C. Liang, P. Zou, A. Nairan, Y. Zhang, J. Liu, K. Liu, S. Hu, F. Kang, H.J. Fan, C. Yang, Exceptional performance of hierarchical Ni-Fe oxyhydroxide@NiFe alloy nanowire array electrocatalysts for large current density water splitting, *Energy Environ. Sci.* 13 (2020) 86–95, <https://doi.org/10.1039/C9EE02388G>.